

The Wavefront Aberration Function of Normal Human Corneas

5.1

INTRODUCTION

5.1.1 Current knowledge of the normal corneal aberrations

In order to completely understand the eye's optical system and correct its errors by reshaping the cornea, the aberrations of the whole eye, as well as those contributed only by the cornea, should be known. The front of the cornea is the single most important optical surface in the eye, and any modification of its shape, as in refractive surgery, can have a significant effect on the optics of the entire system. Our knowledge of the aberrations of normal corneas is still limited because, until recently, there was no practical means to measure the surface shape of the cornea with sufficient accuracy or detail. The new technology of computerized videokeratography has recently made highly accurate measurement possible, and from this, its corneal aberrations can be studied in detail.

In spite of the large number of articles and books on corneal topography, relatively little research has been done to study aberrations of the normal cornea. In one study of nine normal eyes, Howland *et al.*, found that, on average, these corneas had a slight negative spherical aberration, though this was not true for all subjects (Howland, Buettner, & Applegate, 1994). Hemenger estimated the wavefront aberration for one cornea, and found 2 wavelengths (λ) of positive spherical aberration at the edge of a 5.5- mm pupillary zone (Hemenger, Tomlinson, & Oliver, 1994). Other studies (Carney & Henderson, 1993; Applegate, *et al.*, 1994b; Carney, Mainstone, & Henderson, 1997) have suggested that highly myopic eyes tend to have higher p values^a (more spherical), and this would result in greater positive spherical aberration. Beyond astigmatism, asymmetric aberrations such as coma are also expected, and the cornea may be the major

^a The "p value" describes the shape of a conic section and is related to eccentricity (e) by the formula, $p = 1 - e^2$. A sphere has a p value of 1.0, and p values between 1.0 and 0 describe flattening ellipses. See Chapter 3 for more information on typical p values for human corneas.

source of asymmetric aberrations for the eye as a whole (Howland, *et al.*, 1994). Hemenger (1994) found “substantial” corneal coma based on topography data for one cornea, though the amount of coma was not quantified.

Several studies (Camp, Maguire, Cameron, & Robb, 1990; Maguire, Zabel, Parker, & L, 1991; Maguire, Camp, & Robb, 1993) used computer ray tracing to evaluate the optical quality of real corneas. They did not compute wavefront aberrations functions, but rather point spread functions based on data from a first-generation computerized videokeratoscope, the CMS (Corneal Modeling System). Camp convolved the point spread functions with both high and low contrast Snellen letters to create simulated images for several normal and abnormal corneas. These demonstrated the degree to which image quality would be degraded as a result of keratoconus and epikeratophakia. Using similar methods, Maguire evaluated optical quality for five PRK eyes three months after surgery. The simulated images of high to low contrast Snellen letters showed reduced image quality for lower contrast letters.

In recent years, more research has been done to study the effect of refractive surgery on corneal optical aberrations and visual performance. In the correction of myopia, these procedures flatten the central 5-6 mm of the cornea but leave an abrupt transition to a steeper peripheral region. This is radically different from the natural cornea profile (Applegate, Howland, Sharp, Cottingham, & Yee, 1998), which gradually flattens from center to periphery, and we can expect to see unusual aberrations in eyes which have been modified by refractive surgeries. After both radial keratotomy (RK) and photorefractive keratotomy (PRK), large amounts of positive spherical aberration (Seiler, Reckmann, & Maloney, 1993; Applegate, *et al.*, 1994a; Applegate, Hilmantel, & Howland, 1996; Martinez, *et al.*, 1996; Applegate, *et al.*, 1998) were found, and higher refractive corrections were associated with more severe spherical aberration. These optical results were associated with decreased visual performance, measured by a loss in contrast sensitivity and/or low contrast visual acuity (Applegate, *et al.*, 1995a; Verdon, Bullimore, & Maloney, 1996; Applegate, *et al.*, 1998; Gauthier, *et al.*, 1998; Bullimore, Olson, & Maloney, 1999). Using Zernike analysis of corneal height data following RK, Schwiegerling isolated higher order surface shape aberrations from which he modeled the expected effect on visual performance (Schwiegerling J & JE, 1997). He predicted a reduction in contrast sensitivity which would be most noticeable at mid spatial frequencies. Another study of 50 eyes corrected for -6.00 (D) diopters of myopia with PRK showed significant increases in Zernike spherical aberration and coma and a significant decrease in the MTF, especially between 2 and 15 cycles per degree (Oliver, Hemenger, Corbett, & al., 1997). A study of 22 patients corrected with PRK in one eye and LASIK in the other eye showed significant increases in the wavefront variance, especially with large pupils (Oshika, Klyce, Applegate, Howland, & El Danasoury, 1999). In a normal eye, pupil dilation from 3 to 7 mm causes a 5-6 fold increase in the wavefront variance, but Oshika, *et al.*, found a 25-32 fold increase in post-PRK eyes and a 28-46 fold increase following LASIK.

My ultimate goal was to study the cornea's role in the monochromatic aberrations of the normal eye. This chapter presents my findings for the wavefront aberration of the cornea in isolation from the rest of the eye. Recent improvements in videokeratoscope algorithms have made it possible to measure the corneal surface accurately enough to compute the wavefront aberration function (Chapter 4). The results of this research will add to our still limited knowledge of normal corneal aberrations, and the methods developed here will simplify future analysis of corneal optics.

5.1.2 Wavefront aberration expected for a mean cornea

Since the mean shape of the human cornea is well known (Chapter 3), and the wavefront aberration is directly related to surface geometry, we can predict the average corneal wave aberration function. A first order approximation of the normal human cornea can be modeled by an ellipsotoric surface with an apical radius of 7.80 mm horizontally, 7.65 mm vertically, and a shape factor of $p = 0.8$. Figure 5.1a shows a simulated corneal topography map (axial curvature map) of such a model cornea. The vertically oriented dumbbell pattern is typical of with the rule astigmatism, in this case 0.85 (D). Figure 5.1b shows a surface plot of the corresponding wavefront aberration function for a 5.6-mm-diameter pupil. It has a saddle-like shape due to astigmatism, and the minimum and maximum wavefront values are -0.6 and 6.5 wavelengths respectively. The wavefront aberration for a real cornea would probably show greater asymmetry than this (Howland, *et al.*, 1994). Across the range of normal apical radii and shape factors, and for this pupil size, the spherical aberration could conceivably range from a maximum edge height of -0.25 to 8 ; 1.25 diopters of astigmatism would add about ± 3 wavelengths to this.

5.1.3 Computing the wave aberration function from corneal topography

Three methods may be used to compute the corneal wavefront aberration from a known elevation contour. Using the an elliptical model cornea, the accuracy of the three methods, which I refer to as, ray tracing, the Fermat and the surface aberration methods, were compared.

a. Ray tracing

The basic way to compute the wavefront aberration at discrete points across and optical surface is by ray tracing. In this particular application of ray tracing, the corneal front surface and pupil are considered in isolation from the rest of the eye (Fig. 5.2). Ray tracing based on Snell's law allows us to mathematically construct the optical wavefront that propagates through the pupil after refraction at the cornea. In the case of a theoretical aberration free cornea, the wavefront will be spherical with its radius centered on focal point F. This "pupil sphere" is the reference surface from which wavefront aberrations are measured. If aberrations are present due to the shape of the corneal surface, the actual wavefront will depart

from the pupil sphere, and the optical path distance between these surfaces is the wavefront aberration. The distance is measured along the refracted ray (Hopkins, 1950; Born & Wolf, 1980), which is segment AB in Fig. 5.2. This can be closely approximated by segment CB, which is on a radius of the reference sphere (Welford, 1986). This definition for the wavefront aberration is used by some references (Williams & Becklund, 1989; Smith, 1990). For the range of normal corneal shapes, the difference between distances AB and CB is less than $\lambda/1000$ wavelengths, and defining the aberration as BC simplifies calculations. Multiplying CB by the refractive index converts this physical distance to optical path distance, which can be expressed in micrometers or wavelengths.

Assuming an elliptical corneal profile, with apical radius r and shape factor p , the wavefront aberration may be computed by ray tracing using the following steps (see Fig. 5.2).

- 1) The height of an incident parallel ray, which intersects the cornea at point Q, is defined as y_q .
- 2) From Baker's formula for a conic section (see Eqs. 3-2, 3-5 and 3-6), the x coordinate (x_q) of point Q is computed using Eq. (5-1).

$$x_q = \frac{r - \sqrt{r^2 - py_q^2}}{p} \quad (5-1)$$

- 3) The angles of incidence and refraction at point Q are measured from the surface normal, which is related to the first derivative of Eq. (5-1). In the case of a parallel incident ray, the angle of incidence (θ_i) is equal to the angle which the normal makes with the optic axis. This angle is computed using Eq. (5-2).

$$\theta_i = \text{atan} \left(\frac{y_q}{r - px_q} \right) \quad (5-2)$$

- 4) Using an assumed value for the index of refraction (n), the angle of refraction (θ_r) is computed using Eq. (5-3), which is Snell's law.

$$r = \sin^{-1} \left(\frac{\sin i}{n} \right) \quad (5-3)$$

5) The location of point B on the refracted wavefront can be determined because the angle of the refracted ray is known and the optical distance traveled by the ray from point T to B must be equal to the optical distance that an axial ray travels between the corneal apex (O) and the pupil center (P). Angle θ , which the refracted ray makes with the vertical is,

$$\theta = \frac{r}{2} - i + r, \quad (5-4)$$

and the distance QB is computed from Eq. (5-5). OP represents the physical distance from the corneal apex to the pupil.

$$QB = \frac{n(OP) - x_q}{n} \quad (5-5)$$

The coordinates for point B are then computed from Eqs. (5-6) and (5-7).

$$x_b = (QB)\sin \theta + x_q \quad (5-6)$$

$$y_b = y_q - (QB)\cos \theta \quad (5-7)$$

6) Since the wavefront aberration is defined along the normal to the reference sphere, the wavefront aberration (W) for this ray is:

$$W = (BC)n = (PF - BF)n. \quad (5-8)$$

Ray tracing requires a knowledge of the surface normal. This is easily computed for a model cornea based on a known analytical formula, but for real eyes, the surface normal must be estimated by

approximating the corneal surface with a polynomial and differentiating, or by calculating the cross product of vectors connecting the point of interest and other nearby points. Ray tracing through real corneas, based on videokeratoscope data, can become complex, and it depends on certain assumptions about the surface. These are relative disadvantages for the ray tracing method compared to two simpler methods, which will be described next.

b. Fermat's principle

Fermat's principle of least time, which is the basis for Snell's law and refraction, defines the path taken by a ray of light as that which will take the least time. When light crosses into a medium that has a different refractive index, the least time to travel between two points will not necessarily be a straight line between the points. It will, however, be the shortest optical path, which is defined as the physical distance multiplied by the refractive index. In a hypothetical, aberration-free optical system, any two rays, which depart from a point source in object space and travel through an optical system, will arrive at the image point at the same time, in phase, as shown in Fig. 5.3. That is, the optical path length for a marginal and axial ray must be equal, and the difference between their optical paths will be zero.

$$\text{optical path} = TQ + n(QF) = n(OF) \quad (5-9)$$

If the two optical paths are not equal, the two light rays will not arrive at the image point in phase, and this will indicate that an aberration or phase shift was introduced somewhere along the path. In the case of a single refracting surface such as the anterior cornea, the phase shift must be due to the surface shape. Therefore another definition for the wavefront aberration (W) is the difference in path lengths between a reference ray (in this case the axial ray) and other rays which pass through the surface (Thibos, 1992; Thibos, Ye, Zhang, & Bradley, 1997).

$$W = TQ + n(QF) - n(OF) \quad (5-10)$$

This was the method used by Hemenger (1994) to compute the corneal wavefront aberration from corneal topographic data for one eye. Hemenger also calculated the optical path between the anterior and posterior corneal surfaces to estimate a wavefront aberration for the entire cornea.

This method, which I will refer to as the Fermat method, is simpler than ray tracing because it is not necessary to know the corneal surface normals. The basic data required to compute the wavefront aberration by this method are the coordinates for an object point, its paraxial image point, a corneal reference point (O in Fig. 5.3), and the other surface coordinates. Figure 5.3 illustrates the Fermat method

with a schematic cornea which is symmetric about its optic axis. Here, the corneal reference point (O) is the intersection of the optic axis and corneal surface, but is not necessary that the reference point lie on the optic axis. In the case of real corneas, a better reference point would be the intersection of the line of sight with the cornea. This point is known as the corneal sighting center and is discussed further in Section 5.1.4. The freedom to select any reference point makes the Fermat method versatile, and this was the method that I used to compute the corneal wavefront aberration for my subjects. The relative accuracy of the Fermat method, compared with ray tracing, is discussed in Section 5.1.3d.

c. Surface aberration method

The optical path differences which cause aberrations arise because of the shape of the corneal surface. Therefore, it should be possible to directly calculate the corneal wavefront aberration from the surface data. In the case of a rotationally symmetric cornea, the surface shape that will be free of aberrations is an ellipsoid with an eccentricity (e) equal to the inverse of the refractive index (1/n) (Klein & Mandell, 1995). This is known as a Cartesian oval. Any departure from this surface will result in aberrations. I refer to the relative elevation of the cornea compared to the best fit Cartesian oval as the “surface aberration”, and if this is known, the corneal wavefront aberration can be computed using a very simple formula (Thibos, 1996), which may be derived based on the geometry shown in Fig. 5.4.

For an aberration-free cornea, represented by arc OS, a ray from a distant axial point is refracted at point S and propagates to the focal point, F. In a real cornea (arc OQ) with a surface shape other than the Cartesian oval (arc OS), the optical distance traveled between the object and image points will be aberrant compared to the distance traveled in the aberration-free case. The difference between the aberration-free path through the Cartesian oval and the path taken through the real cornea is the estimated corneal wavefront aberration (W). This is developed in the following equations, which refer to Fig. 5.4. The aberration-free optical path length is represented by

$$TS + (SF)n, \tag{5-11}$$

and the optical path through the real cornea is

$$TQ + (QF)n. \tag{5-12}$$

The difference between this is defined as the wavefront aberration (W) for that ray height.

$$W = [TS + (SF)n] - [TQ + (QF)n]. \tag{5-13}$$

CHAPTER 5: Wavefront Aberration Function of Normal Corneas

Substituting (TS + SQ) for TQ and simplifying, the equation becomes,

$$W = (SF)^n - SQ - (QF)^n. \quad (5-14)$$

Substituting (SA + AF) for SF and simplifying, we get,

$$W = (SA)^n + (AF)^n - SQ - (QF)^n. \quad (5-15)$$

Because the distances, QF and AF are very large compared to QA (Fig. 5.4), distance AF can be approximated by QF without significant loss of accuracy. The equation then converts to,

$$W \approx (SA)^n + (QF)^n - SQ - (QF)^n, \quad (5-16)$$

which further simplifies to,

$$W \approx (SA)^n - SQ \quad (5-17)$$

Segment SA is equal to $SQ(\cos \theta)$, therefore by substitution the equation becomes,

$$W \approx SQ(\cos \theta)^n - SQ, \quad (5-18)$$

and then,

$$W \approx SQ[(\cos \theta)^n - 1]. \quad (5-19)$$

I call segment SQ the “surface aberration”, and angle θ is the angular height of the incident point from the paraxial focal point, F. For the range of normal pupil sizes and corneal curvatures, the value for $\cos \theta$ is between 0.99 and 1.00, so another approximation yields,

$$W \approx SQ(n-1). \quad (5-20)$$

If $n = 1.376$, the corneal wavefront aberration function is simply the surface aberration multiplied by 0.376. Since this method tends to slightly overestimate the wavefront aberration, a slightly smaller value, $n =$

1.363, gives an estimate which agrees more closely with the ray tracing result for the same cornea. Howland and Applegate also noted the same simple relationship between corneal topography and its wavefront aberration function, though they used the keratometer index of 1.3375 (Howland, *et al.*, 1994; Applegate, Nunez, Buettner, & Howland, 1995b). Approximations at several stages are necessary to develop this formula, but it is a simple solution for finding the wavefront aberration directly from corneal topography. The surface aberration method does not require a knowledge of the corneal surface normals and is therefore simpler than ray tracing. For a symmetrical cornea centered on the videokeratoscope axis, the wave aberration computation is straight forward, but computations become more complex if the aberrations must be referenced to point that is not on the optic axis. This is a problem with most real corneas since the line of sight is the preferred reference axis for studying corneal optics, but it usually does not coincide with the videokeratoscope axis. Before the surface aberration method can be used to compute the corneal wave aberration, the corneal data must first be transformed so that the line of sight becomes the central reference axis.

Once the corneal elevation data is centered on the desired reference axis, the wave aberration may be computed by the following steps.

- 1) Starting with the mean apical radius and assumed index of refraction, compute the Cartesian oval, which will be the reference surface.
- 2) Compute the elevation difference between the cornea and the reference surface.
- 3) If Eq. (5-19) will be used, compute the angle θ , and solve for the wavefront aberration. Equation (5-20) can also be used to compute the wave aberration directly from the elevations.

d. Three methods compared

Formal computation of the wavefront aberration function requires ray tracing to construct the refracted wavefront in the pupil. This is difficult to implement with real corneal data because corneal topography instruments do not provide information on the surface normals at the sampled points. The Fermat and surface aberration methods are advantageous since they can compute the corneal aberrations directly from elevation data without the normals. I tested the accuracy of the Fermat and surface aberration methods relative to ray tracing, using mathematical model corneas that had elliptical parameters similar to my subject's corneas. Ray tracing is considered the "gold standard" in this computation of the wavefront aberration since it is based on a direct application of Snell's law to the cornea, without approximations or assumptions. You would expect to have the greatest error for corneas with steep apical radii and high p values, therefore I selected reasonable worse case parameters for each of my subjects, and applied these to the wavefront computations. Since the model corneas were symmetric and centered, only spherical

aberration was present, and the maximum aberration occurs at the pupil edge. Results of the comparison are summarized in Table 5.1. Both the Fermat and surface aberration methods gave identical answers, which departed from the ray tracing answer by less than $\lambda/10$ or about 1.3% of its value. The negligible difference between the ray tracing result and that of the other two methods is probably due to subtle differences in the basic definitions of the wavefront aberration used by the different methods. For the purposes of my research, the agreement is close enough that I can consider the wave aberrations computed by all three methods as equivalent. The Fermat method was selected used in this study since it allows direct computation of the corneal aberrations even when the line of sight is not centered on the corneal topography data.

TABLE 5.1 Comparison of the three methods for computing the spherical aberration (W) for an elliptical model cornea. Corneal apical radii and shape factors were chosen to estimate the theoretical maximum spherical aberration for each subject. Pupillary diameters were 5.6 mm. Distances from the corneal apex to the pupil plane were 3.04 mm for AB and DH and 3.84 for LT. Maximum wavefront aberrations in wavelengths ($\lambda = 633$ nm) were computed by ray tracing, the Fermat, and surface aberrations methods. Error, expressed in wavelengths and percent indicate how much the wavefront computed by the Fermat and surface aberration methods differed from ray tracing.

Subject	Apical radii (mm)	Shape factor (p)	W by Ray tracing (λ)	W by Fermat (λ)	W by Surface aberration (λ)	Fermat/Surf Error (λ)	Fermat/Surf Error (%)
AB	7.7	1.0	5.69	5.74	5.74	.05	0.8
DH	8.2	1.0	4.67	4.70	4.70	.03	0.7
LT	7.7	1.1	6.79	6.88	6.88	.09	1.3

5.1.4 Central reference axis for corneal optics

Before we can correctly compute the cornea wave aberration from videokeratoscopic data using instruments such as the EyeSys Corneal Analysis System or the Tomey TMS-2, another fundamental consideration must be addressed. About which corneal reference point and reference axis should the corneal elevations be measured? Vision science has defined several major reference axes of the eye, such as the visual axis (foveal achromatic axis), pupillary axis and line of sight, but for this study of the eye's aberrations, the reference axis should be the line of sight (Mandell, 1992; Mandell, Chiang, & Klein, 1995; Applegate, *et al.*, 2000—In press). The line of sight, also referred to as the fixation axis, is the line which connects the center of the entrance pupil with the fixation point. It is the chief ray of the pencil of light coming from the point of fixation, which is limited by the pupil, and after passing through the eye's

optics, terminates on the fovea. This study is concerned with the optics of foveal vision, and since the wavefront aberration function is centered on the pupil, the logical reference axis is the line of sight. The visual axis, which runs between the fixation point and fovea, through the nodal point, is useful for other purposes, such as calculating image magnification, but it is not the reference axis needed for this study.

During normal videokeratoscope alignment, the patient fixates a small light located at the center of the Placido disk pattern, and as required by the surface reconstruction algorithm, the instrument optic axis (FC in Fig. 5.5) must be normal to the cornea. The optic axis of the instrument is therefore directed toward the corneal center of curvature (C), but this does not necessarily pass through the center of the entrance pupil (E). In fact, in most cases, as shown in Fig. 5.5, the entrance pupil center is slightly displaced from the videokeratoscope axis, and the line of sight (FE) is displaced from the videokeratoscope axis. The point where the line of sight intersects the corneal surface (S) is called the corneal sighting center, and Mandell recommends that, for the purposes of studying corneal optics, the videokeratographic data should be centered on the corneal sighting center (Mandell, 1992; Mandell & Horner, 1993; Mandell, Barsky, & Klein, 1994; Mandell, 1995; Mandell, *et al.*, 1995).

If the Fermat method is used to compute the wave aberration, the corneal data can be centered mathematically on the line of sight by defining the reference ray as the ray which travels from a distant object point, on the line of sight, through the corneal sighting center (which is usually decentered in the keratograph) and eventually terminates on the image point. Other rays can be drawn between the object and image points through other corneal points sampled by the videokeratoscope. The optical path differences between the reference ray and all other rays intersecting the cornea defines the wavefront aberration, associated with those intersection points. Coordinates for the corneal sighting center are therefore needed to compute the corneal wavefront aberration. The specific steps I used to determine the corneal sighting center location are described in Section 5.2.6.

5.1.5 Ellipsoid fitting of real corneal topography

Videokeratoscopes do not measure the cornea within the inner ring, and this leaves a 0.5-mm-diameter zone at the center of the cornea which is unsampled. It is possible to estimate the central apical radius based on data obtained from the innermost ring. It is also possible to estimate the apical radius (r) and shape factor (p) for a best fit ellipse of each corneal meridian. Computerized videokeratoscopes, such as the EyeSys Corneal Analysis System, sample thousands of points in a polar grid, meridian by meridian. After acquiring and processing the image, the EyeSys stores data files that contain the radial distance to each sample point (*.RA file) and the axial radius (*.XX file) at each point. Referring to the geometry described in Fig. 3.2 or Appendix B, the radial distance (y) and axial radius (r_a) at any point on an ellipse are related

by Eq. (5-21) (Bennett & Rabbetts, 1989).

$$r_a^2 = (1-p)y^2 + r^2 \quad (5-21)$$

This formula shows that, for an ellipse, a linear relationship exists between y^2 and r_a^2 in which $(1-p)$ is the slope and r^2 is the y intercept. Plotting a linear regression, within each meridian, for r_a^2 (from the *.XX file) as a function of y^2 (from the *.RA file) allows computation of the apical radius (r) and p value for the best fit ellipse for each meridian (Bennett & Rabbetts, 1989; Douthwaite, 1995; Douthwaite, Pardhan, & Burek, 1996) by the following formulae:

$$r = \sqrt{(\text{y intercept})} \quad (5-22)$$

$$p = (1 - \text{slope}) \quad (5-23)$$

These principles were used to determine the p value for the best fit ellipse in each meridian. Once the p value was known, it was possible to compute and compensate for much of the instrument error and thereby improve the accuracy of the surface topography data (see Chapter 4). Section 5.2.5 specifically describes how I implemented this data correction procedure.

5.2

METHODS

After describing the human subjects used for this study, this section will summarize the specific steps I used to compute the corneal wavefront aberration function from measurements of corneal topography using the EyeSys videokeratoscope. The important steps in this process are listed below.

- 1) Calibrate the EyeSys videokeratoscope
- 2) Acquire corneal topography data images
- 3) Compute mean corneal surface elevations
- 4) Correct EyeSys data for instrument bias
- 5) Compute the corneal sighting center location
- 6) Compute the corneal wavefront aberration
- 7) Transform data from polar to Cartesian coordinates

- 8) Fit data to Zernike polynomials

5.2.1 Subjects

The corneal wavefront aberration function for three normal corneas was based on data collected from the EyeSys 2000 Corneal Analysis System, one of the major corneal topography systems used in clinical practice today. The Institutional Review Board approved the research protocol, and informed consent was obtained from the subjects prior to taking measurements. The right eye of three subjects were measured. Clinical data describing these eyes are listed in Table 5.2.

TABLE 5.2 Clinical data describing the right eye of the three subjects.

Subject	Refraction	BVA	Keratometry
AB	+0.88 - 0.50 x 030	20/15	42.51@003 / 43.32 (7.94@003 / 7.79)
DH	+0.13 - 0.38 x 088	20/15	39.85@175 / 40.47 (8.47@175 / 8.34)
LT	-0.63 - 0.88 x 090	20/15	42.83@100 / 43.38 (7.88@100 / 7.78)

5.2.2 Instrument calibration

A preliminary study to verify the accuracy of the EyeSys videokeratoscope is described in Chapter 4. The results of that study indicate that, after compensation for systematic instrument bias, surface elevation measurement error, for the area of the cornea which I would be measuring, could be reduced to less than $\pm 0.25 \mu\text{m}$ (Fig. 4.6). This would lead to an error of approximately ± 7 in the wavefront aberration function. Following the directions in the EyeSys operator's manual, the instrument software was recalibrated prior to taking measurements.

5.2.4 Corneal topography data acquisition

Mandell suggests that patients be given an appropriate peripheral fixation point so that topographic measurements will be centered on the corneal sighting center. For this reason, subject AB was instructed to fixate a point located 1 degree to the left (nasal) and 0.2 degrees below the EyeSys fixation light (Table 5.3 right column). Because of the difficulty in precisely shifting fixation by very small angles, this did not exactly center the corneal sighting center and a slight residual angle remained, which was mathematically compensated for later. Subjects DH and LT were instructed to fixate the central fixation

light, and EyeSys images were taken using standard alignment. Approximately 20 good quality images were acquired for each eye, and data was stored for later processing.

Although the EyeSys instrument uses 18 rings and is designed to measure up to about a 9-mm corneal diameter, it is common for a patient's nose or brow to obstruct portions of the peripheral rings. I attempted to maximize corneal coverage by having subjects turn their faces and open their eyes widely, but still some data was missing from the outer rings. Only complete rings were used in my analysis. Table 5.3 summarizes the number of rings, extent of corneal coverage and number of good images for each subject.

TABLE 5.3 Summary of EyeSys images collected for each subject.

Subject	Number of good rings	Corneal diameter measured (mm)	Number of good images
AB	12	6.2	15
DH	11	6.0	15
LT	13	6.6	19

5.2.4 Surface elevation computation from raw EyeSys data

The standard EyeSys software does not compute corneal elevations since this is not usually used in clinical practice. Upon request the manufacturer provides a utility program entitled, CORSAG18.EXE, which uses input from previously stored data files to compute the elevations. The README file, which accompanies this program, is included in Appendix C. Among the six data files that are normally saved for each image, the two which are needed to compute the surface elevations are the *.XX and *.RA files. The *.XX file contains the axial radius of curvature associated with each sampled point in hundredths of a mm; i.e., 7.89 mm is recorded as 789. The *.RA files records the radial distance of each point from the corneal center, also in hundredths of a mm; i.e., 0.25 mm is recorded as 25.0. Radial distances were approximately 0.25 mm from the videokeratoscope axis to ring #1, and were about 4.5 mm for ring #18. Each of the raw EyeSys data files are organized with a one-line header followed by 360 rows, with 19 numbers in each row. The first number gives the angular meridian (0-359) in degrees. This is followed by 18 numbers, which are the data associated with each EyeSys ring from center to periphery.

The CORSAG18.EXE program, uses the *.XX and *.RA files to compute the surface elevations, which are stored in an ascii text file with a *.SG extension. Elevations in the *.SG files are specified with reference to a plane perpendicular to the instrument axis and tangent to the cornea apex. Data are recorded in

units of tenths of a micrometer; i.e., 1 μm is recorded as 10.0). The raw EyeSys data set for each subject included these three data files for each good image. For example, subject AB had 15 good EyeSys images, and 15 *.XX, *.RA and *.SG files. For each subject I computed a mean *.RA and *.SG file with values scaled to micrometers. A mean *.XX file, scaled to mm, was also computed for each subject. The mean *.XX and *.RA files were used to compute the elliptical shape factor (p value), which was needed to correct the mean *.SG elevation data for systematic instrument error (see Section 5.2.5). Finally, the mean *.RA and *.SG files were used to compute the wavefront aberration (Section 5.2.7).

5.2.5 Correction for systematic instrument error

In the study described in Chapter 4, I discovered that the EyeSys surface elevation data contains an error that varies as a function of the ellipsoid shape factor and increases from the center to periphery of the cornea. The procedure developed in Section 4.4.1 to compensate for systematic instrument error was applied to the elevation data for each subject before computing the wavefront aberration.

It is important to keep in mind that the EyeSys, and all clinical videokeratoscopes, measure corneal topography meridian by meridian, presumably because of the difficulty of implementing a true three-dimensional reconstruction algorithm. In effect the three-dimensional corneal surface is treated as a set of 360 two-dimensional slices. In compensating for EyeSys error, I retained the two-dimensional approach and corrected the data meridian by meridian, using the process which I will describe next.

The steps required to correct the EyeSys surface elevation data (mean *.SG file for each subject) were:

- 1) Compute the square of each of the axial radius values, which were contained in the mean *.XX data file. Each subject's mean *.XX file was organized into 360 rows (one for each radial meridian) and within each meridian there were 11-13 axial radius values, depending on the subject. This step yielded a data array with 360 rows, and in each row there were 11-13 squared radius values.
- 2) Compute the square of the radial distances contained in the mean *.RA data file. This step also produced a data array with 360 rows, each of which had 11-13 squared distance values.
- 3) For each meridian, there was now a data vector of squared axial radii (r_a^2) values and another data vector of squared radial distance values (y^2), which, as described in Section 5.1.5, are related by Eq. (5-21), which is repeated here.

$$r_a^2 = r_0^2 + (1 - p)y^2 \quad (5-21)$$

CHAPTER 5: Wavefront Aberration Function of Normal Corneas

Variable r_0 represents the apical radius of curvature, and p is the elliptical shape factor. Solving for the slope of the linear regression between r_a^2 (ordinate) and y^2 (abscissa), as described in Section 5.1.5, I found the elliptical shape factor (p) for each meridian according to Eq. (5-23), which is also repeated here.

$$p = (1 - \text{slope}) \quad (5-23)$$

4) Knowledge of the p value allowed me to compute components for a linear equation that would be used to estimate the fractional sag error (FSE) of the EyeSys instrument. The linear equation was composed of a slope and an intercept, both of which were computed based on the p value, by the following formulas. Equations (5-24) and (5-25) are the same as Eqs. (4-12) and (4-13) respectively.

$$\text{slope} = 0.003165 \times p - 0.003445 \quad (5-24)$$

$$\text{intercept} = -0.003664 \times p - 0.0003363 \quad (5-25)$$

5) Using the linear equation build from the slope and intercept components computed in the previous step, I computed the fractional sag error (FSE), which is defined as the sag error divided by the measured sag (Eq. 4-11), using Eq. (5-26). Equation (5-26) is the same as Eq. (4-14). Variable d represents the radial distance of each EyeSys sampled point from the optic axis and was contained in the mean *.RA files.

$$\text{FSE} = \text{slope}(d) + (\text{intercept}) \quad (5-26)$$

6) With a value for the FSE, I computed a corrected a corrected sag (CS) for each measured sag value contained in the *.SG file according to Eq. (5-27), which is the same as Eq. (4-15).

$$\text{CS} = \text{measured} \times (1 - \text{FSE}) \quad (5-27)$$

I imported the basic data arrays (*.XX, *.RA and *.SG) into an Excel spreadsheet and applied each

of the steps listed above to each meridian of data. The end product was a data array with the corrected surface elevations, in micrometers, for each subject.

5.2.6 Compute the corneal sighting center location

I used the Fermat method to compute the corneal wavefront aberration function. In order to center the function on the line of sight, it was necessary to trace a ray from a distant object, located on the line of sight, through the corneal sighting center, to the corresponding image point. An important intermediate step, therefore, was to determine the location of the corneal sighting center.

In order to compute the three-dimensional coordinates for the corneal sighting center, I needed to know the corneal apical radius, horizontal and vertical angle lambdas^b, distance to the entrance pupil and distance from the cornea to the EyeSys fixation light. Mean corneal apical radii were provided by the EyeSys simulated keratometer function. To measure angle lambda, an apparatus similar to that described by Mandell (1995) and illustrated schematically in Fig. 5.6, was constructed. A micrometer attached to a slit-lamp biomicroscope was used to measure the distance from the corneal surface to the entrance pupil. Side alignment cameras on the EyeSys ensure that the corneal apex is always in the same location during measurements, and the distance from this point to the fixation light is 119 mm. Table 5.3 summarizes the basic parameters used to compute the location of the corneal sighting center for each subject.

TABLE 5.3 Parameters used to compute the location of the corneal sighting center for the right eye of each subject. Angle lambda is expressed in degrees. A positive horizontal angle means the pupillary axis is temporal to the line of sight. Positive vertical angle means the pupillary axis is below the line of sight. The fixation angle (in degrees) shows where each subject fixated with respect to the EyeSys optic axis.

Subject	Horizontal lambda	Vertical lambda	Entrance pupil (mm)	Cornea mean apical radius	Fixation angle
AB	+1.09	+0.59	2.50	7.87	1.0 nasal & 0.2 down
DH	+0.47	-0.60	2.50	8.41	On axis
LT	-2.34	-2.26	3.27	7.83	On axis

Using this data, the x and y coordinates for the corneal sighting center were computed based on the geometry of Fig. 5.5, where angle lambda is represented by variable λ , the entrance pupil distance is segment SE, the corneal apical radius is segment VC, and the distance from the cornea to the videokerato-

^b Angle lambda is defined as the angle between the line of sight and the pupillary axis. The line of sight joins the fixation point and the entrance pupil center. The pupillary axis is the line which passes perpendicular to the cornea and through the center of the entrance pupil.

scope fixation light is represented by segment FV. The following steps were be used.

- 1) Compute the length of arc PF.

$$(\text{arc PF}) = (\text{FS} + \text{SE}) \quad (5-28)$$

- 2) Find the length of arc SA.

$$(\text{arc SA}) = \frac{\text{SE}}{(\text{FS} + \text{SE})} (\text{arc PF}) \quad (5-29)$$

- 3) Find the length of arc AV

$$(\text{arc AV}) = \frac{\text{VC}}{(\text{FV} + \text{VC})} (\text{arc PF}) \quad (5-30)$$

- 4) Compute angle VCS.

$$\text{VCS} = \frac{(\text{AV} - \text{SA})}{\text{VC}} \quad (5-31)$$

- 5) Finally, the displacement (x) of the corneal sighting center (S) form the videokeratoscope axis (FC) is,

$$x = (\text{VC})\tan(\text{VCS}). \quad (5-32)$$

This procedure was used to compute both the x and y coordinates of the corneal sighting center relative to the apex of the cornea (V). The z coordinate was then computed based on Baker's ellipse equation (Eq. 5-1) and a knowledge of the corneal apical radius and p value. Coordinates for the corneal sighting center relative to the center of the keratographs are listed in Table 5.4.

TABLE 5.4 Estimated position of the corneal sighting center, in mm, relative to the center of the EyeSys corneal topography map. The x and y dimensions refer to standard Cartesian coordinates on the map. Negative z refers to distances behind the corneal apex.

Subject	x	y	z
AB	0.082	0.003	0.000
DH	-0.046	0.057	0.000
LT	0.173	0.171	-0.004

5.2.7 Compute the corneal wavefront aberration function

The Fermat method, described in Section 5.1.3b, was chosen to compute the wavefront aberration. In addition to the corneal surface data, the three-dimensional coordinates for an object point, the corneal sighting center, and the paraxial image point were required to compute the optical path length for the chief ray and other rays. The chief ray was defined as the ray between the object and image point, which passed through the corneal sighting center. The object point was a hypothetical fixation point located 10,000 meters in front of the cornea, on the line of sight, and for my purpose, it was essentially located at optical infinity. The object point and corneal sighting center coordinates defined an incident chief ray, and using an estimated normal to the corneal surface at the corneal sighting center, I used skew ray tracing (Freeman, 1990), through two paraxial surface points, to determine the paraxial image point. Once these points were known, I was able to compute the optical path length for the chief ray. The path length between the object and image points through the other known corneal surface point were also computed, and the optical path difference between the chief ray and each ray through the other corneal points was the corneal wavefront aberration at each surface point. A MATLAB program, which I used to compute the wavefront aberration function, given the object point, corneal sighting center and image point coordinates, is included as Appendix D.

5.2.8 Polar to Cartesian transformation

Up to this point all corneal data had been organized on a polar grid, but in preparation for later comparison with Shack-Hartmann wavefront data (Chapter 7), it was necessary to interpolate the corneal wavefront data to a Cartesian grid. Unless the corneal surface is perfectly symmetrical about the instrument optic axis, the reflected EyeSys rings will not be perfectly circular, and the instrument will measure points located on an irregular polar grid with radial spacing that varies with each meridian. A cubic spline interpolation was fitted to the data within each meridian to interpolate data to a regular polar grid (see

Appendix D). Data points were radially spaced at every 0.1 mm for 360 meridians on this regular polar grid. Next, using Transform 3.3 (Fortner), the polar data was interpolated to a square Cartesian grid with 0.2-mm spacing, which was centered on the line of sight.

5.2.9 Fitting to Zernike polynomials

In order to match the pupil sizes measured with the Shack-Hartmann device (Chapter 7), the corneal data was limited to a 5.6-mm-diameter pupillary zone for subjects AB and LT, while a 5.2-mm zone was used for DH. A MATLAB program was used to fit the wavefront data to a series of Zernike polynomials, which included terms up to the tenth order. A copy of MATLAB program used for Zernike analysis is included in Appendix E. The wavefront data was expressed in wavelengths ($\lambda = 633$ nm).

5.3

RESULTS

5.3.1 Quality of the data

Example corneal topography maps for each subject are shown in Figs. 5.7-5.9. Chapter 4 established that the EyeSys topography system is accurate enough to estimate the corneal wavefront aberration to within $\pm 1/7$ across most of the central cornea. The repeatability (precision) of surface elevation measurements is shown by Figure 5.10, which plots the radially averaged standard errors, as a function of radial distance for the three subjects. Standard errors increased from center to periphery and reached a value of about $0.6 \mu\text{m}$ at $2800 \mu\text{m}$ from the center (5.6-mm-diameter pupil). If the confidence interval for the mean surface elevation is defined as ± 2 standard errors, at the edge of the pupil where variability was largest, the confidence interval was $\pm 1.2 \mu\text{m}$. This means that the confidence interval for the corneal wavefront aberration computed from mean EyeSys sags was $\pm 2/3$ or better across the measured pupil. Wavefront errors equivalent to the standard errors are shown along the right side of Fig. 5.10a. Fig. 5.11 shows the radially averaged signal-to-noise ratio (SNR), which is defined as the mean surface elevation, divided by the standard deviation. The SNR increases from center to periphery, indicating that the instrument's relative precision improves peripherally. This is fortunate since variability is larger near the pupil edge. The increasing SNR from center to periphery may be due to the fact that the instrument makes use of larger images and steeper reflection angles when analyzing peripheral corneal data.

Ultimately the corneal wavefront aberrations would have to be compared to the ocular eye aberrations measured by the Shack-Hartmann system. Since the Shack-Hartmann data was sampled on a regular Cartesian grid, and since it is easier to fit regular Cartesian data to Zernike polynomials, the EyeSys data, which was sampled on an irregular polar grid was interpolated to regular cartesian coordinates. The

interpolated data was then fitted to Zernike polynomials, and the end product of this process, 66 Zernike coefficients, could be used to analyze or synthesize the wavefront aberration. To test how well the Zernike coefficients fit the interpolated data, I compared the wavefront which was reconstructed using the Zernike coefficients with the interpolated data to which the Zernike polynomials had been fitted. The RMS differences between the two wavefronts, listed in Table 5.6, are $\lambda/20$ or less for all subjects. In addition, the ratio of wavefront variances (reconstructed / fitted data) are also listed. These statistics show that the Zernike polynomial fit using 66 modes (10 orders) very closely matched the input data and any error introduced by Zernike fitting was well below measurement error for the original data.

TABLE 5.6 Comparison of wavefronts reconstructed using 66 Zernike polynomials, which had been fitted to interpolated wavefront data, to the input data. The RMS difference between the reconstructed wavefront and fitted data, in wavelength ($\lambda = 633$ nm), is listed for each subject. The reconstructed wavefront variance divided by the fitted wavefront variance is also shown.

Statistic	AB	DH	LT
RMS difference: reconstructed vs actual wavefront (λ)	0.05	0.02	0.03
Ratio of wavefront variances	1.01	.99	.99

How faithful was the Zernike fit to the original raw EyeSys data? To assess this, I used the Zernike coefficients to reconstruct the wavefront on the same points originally sampled by the EyeSys (polar grid with irregular radial spacing). Using data for one subject (LT), the reconstructed wavefront was compared to the wavefront aberration computed directly from the original EyeSys data. The RMS difference between the two wavefronts was $\lambda/33$ for a 5.6-mm pupillary zone. Figure 5.12 shows contour plots of the two wavefronts superimposed. Near the center of the cornea, very small wavefront height variations were smoothed out by the data processing, but they were $\lambda/20$ or less. For the rest of the cornea, the two wavefront are essentially identical.

A Gram-Schmidt orthogonalization can also be used to transform irregularly sampled polar data prior to Zernike polynomial fitting, and this is the process used by Schwiegerling (1995) to decompose corneal elevation data to Zernike polynomials. He tested the accuracy of the Gram-Schmidt orthogonalization plus Zernike fitting routine with simulated corneal data and found an RMS error of less than $0.02 \mu\text{m}$, which equates to about $\lambda/100$ in the wavefront aberration. This is nearly the same magnitude of fitting error that I found following data interpolation, and this demonstrates that any error contributed by either interpolation or Gram-Schmidt orthogonalization is insignificant compared to the measurement accuracy of the original data.

5.3.2 Total corneal wavefront aberrations

Subsequent results are based on the wavefront aberrations determined by reconstruction using the Zernike coefficients. A complete list of the 66 Zernike coefficients for each subject may be found in Appendix F.

The wavefront aberration for each subject was reconstructed after removal of piston, tilt, and defocus. The major components of this “total” wavefront aberration were astigmatism and residual aberrations up to the tenth order. Figure 5.13, shows contour and surface plots of the wavefront aberration functions for the three subjects. Table 5.7 lists parameters which summarize the wavefronts.

TABLE 5.7 Summary statistic describing the total corneal wavefront aberration functions. Piston, tilt and defocus were removed and the “total” wavefront consisted of astigmatism plus aberrations up to the tenth order. The wavefront aberrations were measured in wavelengths ($\lambda = 633 \text{ nm}$).

Subject	Pupil diameter (mm)	Wavefront magnitude (λ)	Total Wavefront variance	Astigmatism variance	Astigmatism % of total variance
AB	5.6	-2.66 to 3.67	1.54	1.41	91.8
DH	5.2	-1.84 to 2.52	0.40	0.31	77.5
LT	5.6	-1.67 to 2.35	0.45	0.31	68.9

From the appearance of the maps and the wavefront statistics in Table 5.7, it is clear that astigmatism is the largest component (69-98%) of the total corneal wavefront aberration for all three subjects. In comparison, the higher order aberrations in these normal eyes are small. To get a better feel for the amount of astigmatism contained in these wavefronts, the Zernike coefficients for primary astigmatism (modes 4 and 6) were converted to ophthalmic prescription notation in the following steps.

The polar form of the Zernike polynomials that represent astigmatism are shown by Eq. (5-33) for mode 4 (astigmatism with axis at 45° or 135°) and by Eq. (5-34) for mode 6 (astigmatism with axis at 90° or 180°). For both modes, the maximum and minimum wavefront heights (s ; in μm), which are at the pupil edge, may be computed using Eq. (5-35), where a is the Zernike coefficient.

$$W = a_4 \sin^2 \theta, \quad (5-33)$$

$$W = \frac{1}{2} a^2 \cos 2\theta, \quad (5-34)$$

$$s = a \sqrt{\frac{1}{6}} (.633), \quad (5-35)$$

This may be converted to diopters (D) using the sag formula:

$$D = \frac{2s}{\sqrt{y^2 - s^2}} (1 \times 10^6) \quad (5-36)$$

Converting both Zernike coefficients for astigmatism to diopters and combining the crossed cylinders, the corneal astigmatism for each subject was computed. (See Section 2.4.5.) The corneal astigmatism represented by the Zernike coefficients are summarized in Table 5.8. For comparison, the EyeSys simulated keratometer values are also shown. The power and axis values obtained by the two methods are in close agreement.

Strictly speaking, a more perfect transformation of the Zernike astigmatism coefficients to the clinical notation requires that the higher astigmatic terms contained in orders 4, 6, 8, and 10 also be included (Schwiegerling, *et al.*, 1995). This is because ophthalmic astigmatism is circular in profile along the major meridians, while the Zernike profiles are parabolic, and a large number of parabolas must be summed to better approximate a circle. For my purposes, the higher order coefficients were small enough that they can be ignored, and for the relatively shallow curvature of these wavefronts, the astigmatic profiles across these pupils can be considered nominally circular (Webb, 1992).

TABLE 5.8 Corneal astigmatism in minus cylinder form, derived from the Zernike coefficients and those computed by the EyeSys simulated keratometry function.

Subject	Zernike coefficients	EyeSys simulated keratometry
AB	-0.94 x 013	-0.82 x 003
DH	-0.54 x 175	-0.62 x 175
LT	-0.47 x 108	-0.55 x 100

5.3.3 Higher order corneal wavefront aberrations

Higher order aberrations are defined here as the aberrations contained in orders 3-10, which are beyond the clinically correctable optical defects. These results differ from those described in the previous section in that astigmatism has been removed. Plots of the higher order aberrations are shown in Fig. 5.14, and certain aspects are summarized in Table 5.9. Various combinations of Zernike spherical aberration, coma and other aberrations were present in the three subjects, and in each case the resulting wavefront surfaces have unusual asymmetric shapes. Because spherical aberration and coma are relatively familiar aberrations, their relative contributions to the higher order wavefront aberrations are listed. Aberrations other than spherical aberration or coma make significant contributions to the wavefront aberration for all subjects. Note that the Zernike terms that are labelled “spherical aberration” or “coma” are not the same as the corresponding classic Seidel aberrations. For example, Seidel primary spherical aberration increases monotonic from the pupil center to its edge, but the Zernike primary spherical aberration is high in the center, decreases in the mid-periphery and then sharply increases at the edge of the pupil. The Zernike spherical aberration term contains a constant which shifts the wavefront away from a mean value of zero, while the other modes have mean wavefront values equal to zero.

TABLE 5.9 Summary statistics for the higher order corneal wavefront aberrations. The contribution of certain aberrations to the higher order wavefront variance are listed to show the relative contribution of each.

Subject	Wavefront magnitude ()	Wavefront variance	1° + 2° spherical aberration contribution (%)	1° + 2° coma contribution (%)	Contribution of other aberrations (%)
AB	-0.74 to 1.88	0.13	45.9	3.3	50.8
DH	-0.62 to 1.20	0.09	13.1	63.9	23.0
LT	-0.91 to 1.92	0.14	62.4	1.8	62.3

5.3.4 Higher order corneal wavefront by order and mode

Figure 5.15 compares the relative contribution of each Zernike order to the higher order aberrations in terms of percentage of the total wavefront variance. Third order aberrations include modes 7-10 (triangular astigmatism and primary coma); fourth order aberrations include modes 11-15 (spherical aberration and others). Table 5.10 shows the cumulative percentage of total wavefront variance as additional orders are added. Over 90% of the aberrations are accounted for in the third and fourth orders and the addition of fifth order (up to mode 21) aberrations accounts for 95% of the aberrations. Ten orders are able to account for 100% of the total wavefront variance in the reconstructed wavefronts, which account for

99% of the variance in the fitted data.

The bar graphs in Figs. 5.16, 5.17, and 5.18 show the relative contribution, in percent, of each of modes 7-21 (orders 3,4,5) to the higher order wavefront variance. The relative contribution of individual modes between 22-66 are insignificant, so they are not shown. In AB modes 7 and 10 combine to form triangular astigmatism, which contributes to 38% of the wavefront variance. The values for this aberration range over ± 0.6 wavelengths. Primary spherical aberration, represented by mode 13, contributes 45% and has minimum and maximum values of -0.3 and +0.5 wavelengths respectively. All other aberrations combined make up about 18% of the total variance. The contour plots in Fig. 5.19 illustrate how the major aberration components sum to form the total higher order wavefront aberrations.

TABLE 5.10 Cumulative contribution of each order to the higher order wavefront variance. Numbers indicate percent of the higher order wavefront variance. The wavefront reconstructed closely matched the original wavefront data (see Table 5.6). The ratio of the variances of the reconstructed wavefront to the input data are also shown.

Order	Modes	AB	DH	LT
3	7 - 10	40.8	74.0	11.0
4	11 - 15	93.73	95.8	93.1
5	16 - 21	95.1	98.9	95.9
6	22 - 28	97.6	99.3	97.9
7	29 - 36	98.9	99.6	98.5
8	37 - 45	99.4	99.8	99.2
9	46 - 55	99.8	99.9	99.6
10	56 - 66	100.0	100.0	100.0
Reconstructed : input wavefront variance ratio		1.01	.99	.99

Figure 5.17 reveals that the dominant aberration for DH is primary coma, which is the sum of modes 8 and 9. Primary coma accounts for 64% of the wavefront variance and minimum and maximum values are ± 0.7 wavelengths. The next largest contribution is made by mode 13, primary spherical, which accounts for 13% of the wavefront variance. The extreme values for primary spherical in DH are -0.1 and +0.2 wavelengths. The other aberrations combined contribute to about 24% of the total aberrations. Figure 5.19 shows how these components, plus the other aberrations sum up to form the total wavefront aberration.

TABLE 5.11 Summary of major components of the higher order wavefront aberrations for three subjects.

Subject	Dominant modes	Description	% of wavefront variance	Min/max values ()
AB	7 + 10	triangular astigmatism	37.6	± 0.63 -0.27 to 0.54
	13	1° spherical aberration	44.5 (remainder 17.9)	
DH	8 + 9	1° coma	63.8	± 0.67 -0.11 to 0.22
	13	1° spherical aberration	12.6 (remainder 23.6)	
LT	13	1° spherical aberration	62.3	-0.32 to 0.65 ± 0.51
	11 + 14	quadrilateral astig	18.4 (remainder 19.3)	

The breakdown for subject LT is show in Fig. 5.18. Primary spherical aberration far exceeds all other components, accounting for 62% of the wavefront variance. The minimum and maximum values of this aberration in isolation are -0.3 and 0.6 wavelengths. Mode 14, which I refer to as quadrilateral astigmatism, contributes 18% to the total variance and has a range of ± 0.5 wavelengths. All other aberrations combined make up about 19% of the total aberrations. Figure 5.19 shows contour plots of these components and their sum. Table 5.11 summarizes the dominant aberration components for each subject.

5.4 DISCUSSION

The methods used in this project enabled me to obtain an accurate picture of the corneal wavefront aberration, centered on the line of sight, for three normal subjects. Although the ultimate goal is to compare corneal aberrations with those of the whole eye, a study of the corneal aberrations in isolation from the rest of the eye gives valuable insight into the characteristics of this important optical component.

For the three subjects, the magnitude of the total wavefront aberrations (including astigmatism) were in the range expected from model eye calculations. When corneal astigmatism (~ -0.50 to -1.00 D) was included in the analysis, the peak to value magnitude of the wave aberrations was about 4-6 μ . In comparison, the higher order aberrations were smaller (1-2 μ), but depending on the subject, they still made up 10-30% of the total wavefront aberration. A common feature in all subjects was that over 90% of the higher order aberrations could be accounted for by the third and fourth orders. All of these subjects had positive spherical aberration, but the relative importance of spherical aberration varied in each eye. In LT

spherical aberration alone contributed to over 60% of the higher order wavefront variance and coma was small, while in DH spherical aberration was relatively small, and coma alone accounted for over 60% of the variance. In all subjects, other Zernike modes besides those associated with spherical aberration and coma played an important role in the total higher order aberrations.

A question when planning this research was, how many Zernike modes should be used to analyze the corneal wavefront aberration? Liang (1992) originally used 15 modes in his analysis of ocular eye aberrations, and Williams later extended his Zernike analysis of ocular eye wavefront data to 66 modes. As shown in Fig. 5.15, the bulk of the aberrations are contained in orders 3 and 4, which includes up to mode 15. The contribution of higher orders diminishes rapidly, but it took 10 orders, or 66 modes to account for 100% of the wavefront variance. This is to be expected for normal healthy corneas with relative smooth contours, but in post-refractive surgery corneas, or in eyes with keratoconus or other diseases, we can expect to see larger aberrations in orders 5-10.

Another question was, Did compensation for the line of sight tilt make a difference in the measured higher order aberrations? To evaluate this, I recomputed the corneal wave aberration for subject LT, who had the largest angle lambda (approximately 3 degrees), using the surface aberration method. This computational procedure is much simpler than the Fermat method, and in effect, it assumes that angle lambda is zero. Table 5.12 lists the Zernike coefficients for selected modes of LT's corneal wavefront aberration, and it compares the results for the Fermat method (with line of sight compensation) and the surface aberration method (no compensation). Differences (right column) for the tilt coefficients (shaded rows) are large, but for the other modes, the value of the Zernike coefficient changed by 0.01 or less. Only the modes with the largest differences are shown. Note that this was for a 5.6-mm-diameter pupil, and the differences would probably be larger for a larger pupil. This analysis shows that, had I ignored line of sight tilt, it would have made little difference in my measurement of the higher order corneal aberrations. The maximum value for angle lambda among my subjects was 3.3 degrees (subject LT). Some articles report average values for angle lambda as large as 9 degrees (Mandell, *et al.*, 1995). Further study is needed to determine if compensation for line of sight tilt can be ignored in normal eyes with large angle lambdas. If so, it would greatly simplify computation of the corneal wavefront aberration from videokeratographic data.

In summary, the higher order wavefront aberrations of normal corneas appear to have peak-to-valley magnitudes of about 2 μm , or about 1.2 μm , and most of the aberrations are contained in the third and fourth Zernike orders. This study does not indicate that either spherical aberration or coma is the major cornea aberration. Both aberrations were present in all subjects, but their relative weights varied with each individual. Aberrations other than spherical aberration and coma were also significant. The techniques developed in this project will simplify future research on the aberrations of normal and abnormal human corneas.

TABLE 5.12 Comparison of subject LT's Zernike coefficients for selected modes when the corneal wavefront aberration was computed using the Fermat method (with line of sight compensation) and by the surface aberration method (without compensation). As expected, coefficients for tilt (shaded rows) are significantly different. For all other modes the difference was 0.01 or less in the value of the Zernike coefficient. The other higher order modes had differences less than 0.01 and are not listed.

Zernike Mode no.	Description	Zernike coefficients		Difference (No comp - With comp)
		With LOS comp	No LOS comp	
1	Horizontal tilt	-0.16	0.06	0.22
2	Vertical tilt	-0.62	-0.40	0.23
4	45/135 astigmatism	0.35	0.34	-0.01
6	90/180 astigmatism	0.49	0.48	-0.01
7	Primary coma	-0.06	-0.07	-0.01
8	Primary coma	-0.14	-0.15	-0.01
13	Primary spherical	0.33	0.33	0.01
25	Secondary spherical	-0.01	0.01	0.01

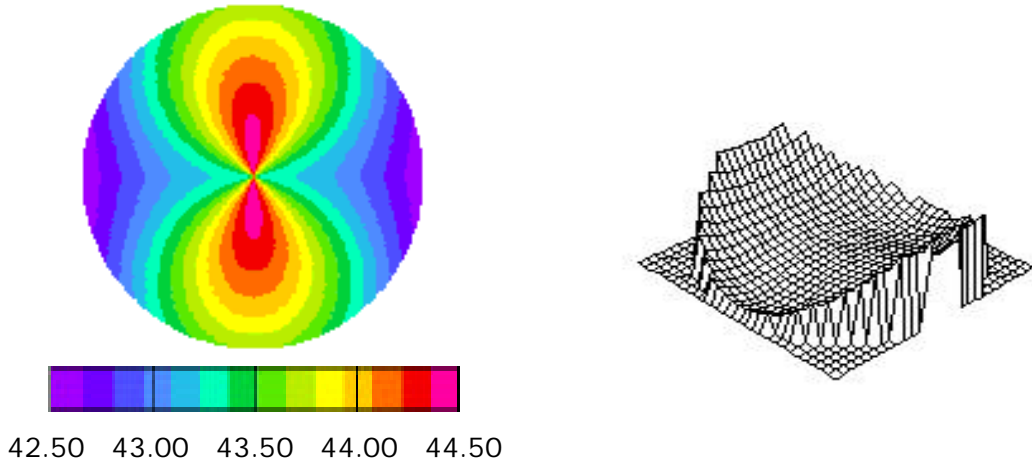


Figure 5.1

Example corneal topography map (left) showing axial curvatures for a model cornea with horizontal and vertical apical radii of 7.80 and 7.65 mm, respectively and with a shape factor of $p = 0.8$. Corneal zone diameter is 5.6 mm. Surface plot (right) of the corresponding wavefront aberration function. Minimum and maximum wavefront values are -0.6 and $6.5 \mu\text{m}$, respectively.

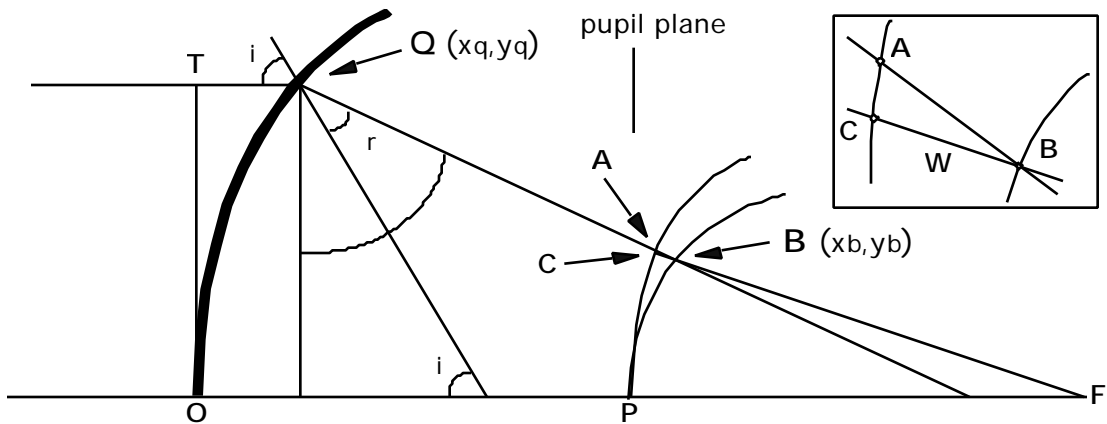


Figure 5.2

Section 5.1.3a explains the steps to determine the wavefront aberration (W) by ray tracing, based on the geometry shown here. The inset clarifies the relationship between points A, B, and C. Some references define W as segment AB, others as CB. For normal corneal dimensions, the difference between the two distances is <0.001 wavelengths. I used the CB definition for W .

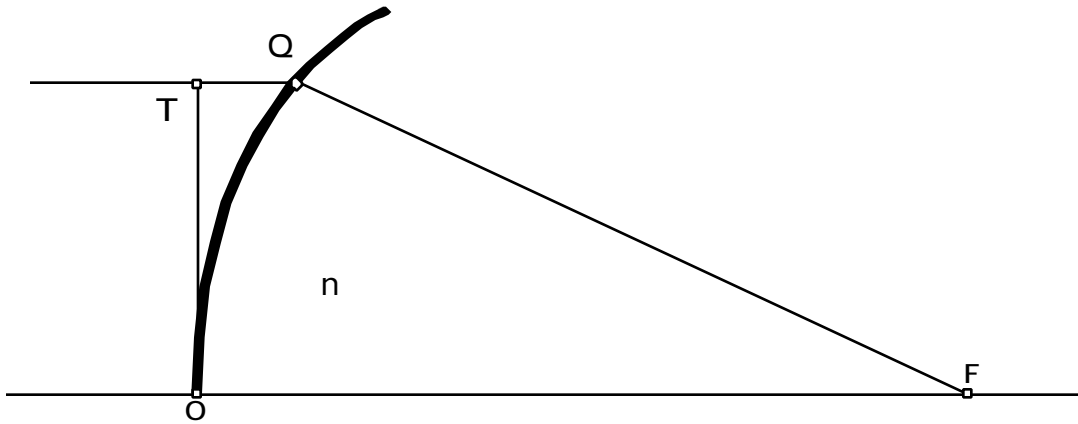


Figure 5.3

This schematic shows that the geometry and requirements for computing the wavefront aberration by the Fermat method (Section 5.1.3b) are much simpler than for ray tracing (Fig. 5.2). The Fermat method makes some approximations, but if the positions of points O, Q, F and the corneal index of refraction (n) are known, an acceptably accurate estimate of the wavefront aberration can be made for normal corneas.

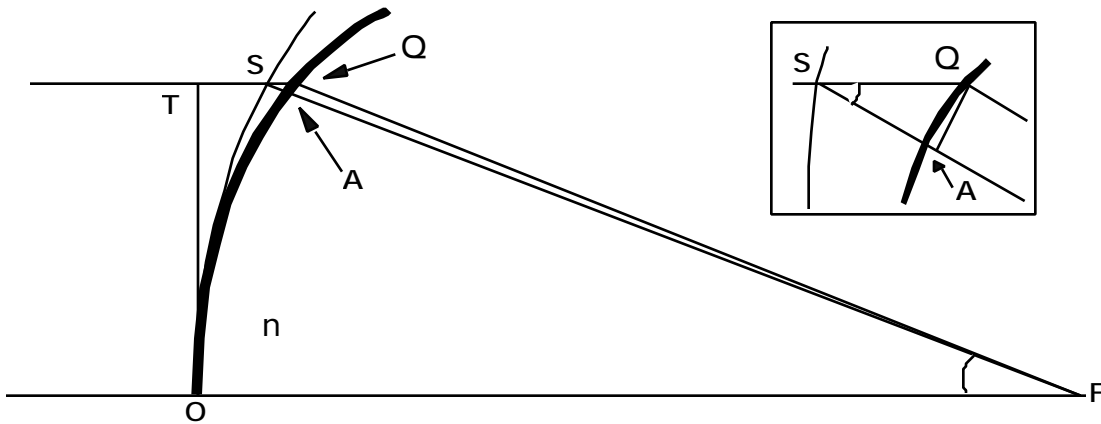


Figure 5.4

The surface aberration method (Section 5.1.3c) is based on Fermat's principle and an approximation that equates distances AF and QF . For most normal corneas, this does not contribute significant error and allows direct computation of the wavefront aberration from distance SQ , which is the "surface aberration" between the Cartesian oval (arc OS) and the cornea (arc OQ). The inset clarifies the relationship between points S , Q , and A .

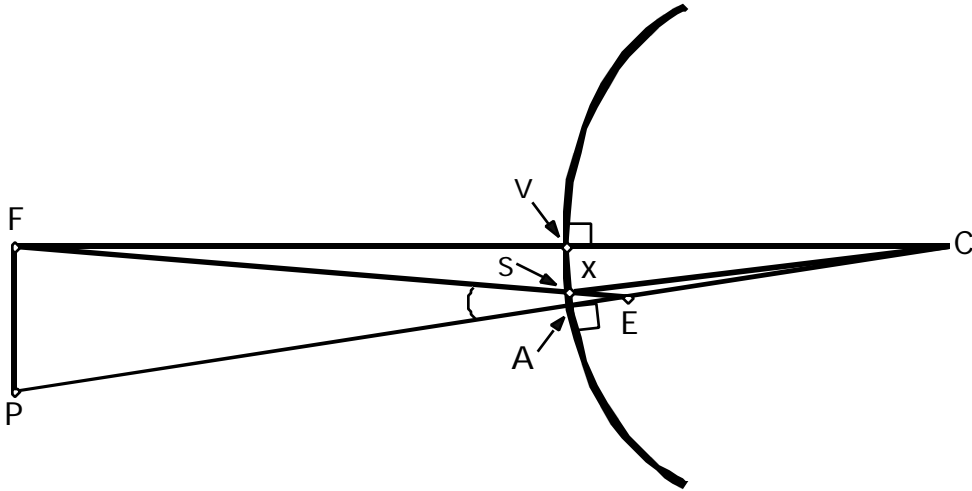


Figure 5.5

During standard videokeratoscope alignment, the patient fixates a light at the center of the keratoscope (F) while the instrument axis (FC) is aligned normal to the cornea. The line of sight (FE) connects the fixation point with the entrance pupil center (E). The pupillary axis (PE) is normal to the cornea and passes through the entrance pupil center. C represents the corneal center of curvature. Corneal topography measurements should be centered on the line of sight, but if angle lambda (λ) is not zero, the line of sight will be displaced. The point where the line of sight intersects the corneal surface is called the corneal sighting center (S), and if its coordinates are known, the corneal wavefront aberration, centered on the line of sight, can be computed (Section 5.1.4). Variable x is the distance from the keratoscope axis to the corneal sighting center (S).

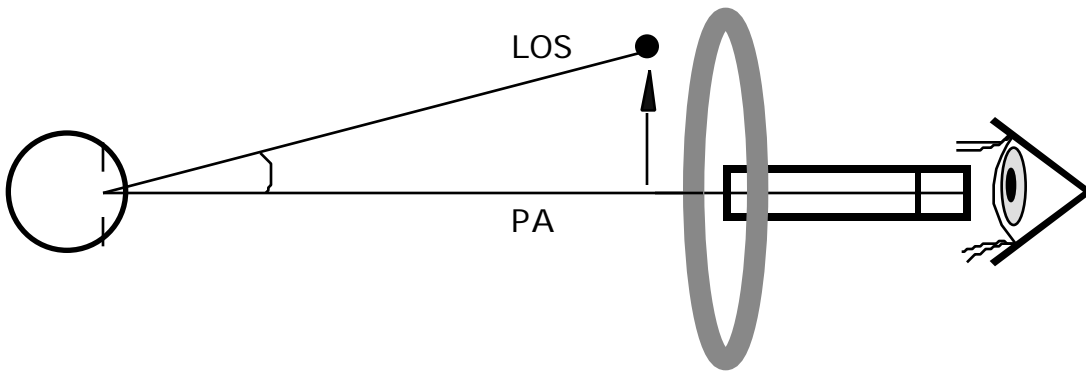


Figure 5.6

The device to measure angle lambda (λ) consisted of an illuminated annulus centered on a short focus telescope. With the subject's head stabilized, the fixation target's position was adjusted until the image of the annulus, reflected off the subject's cornea, appeared to be centered within their pupil. This aligned the subject's pupillary axis (PA) with the telescope axis, while the line of sight (LOS) was directed toward the fixation target. The horizontal and vertical angle lambdas were then easily computed.

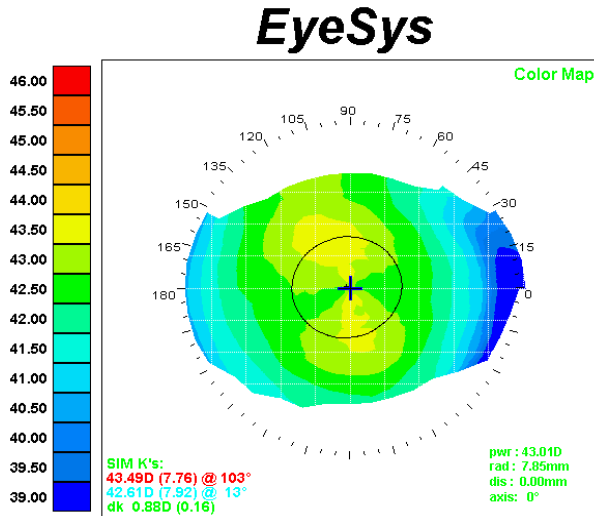


Figure 5.7 EyeSys axial curvature map for AB.

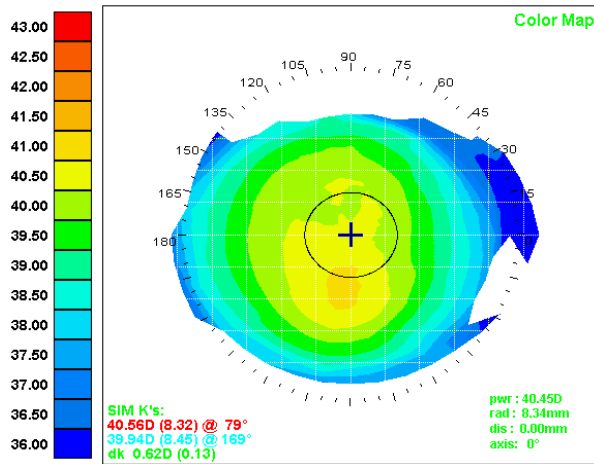


Figure 5.8 EyeSys axial curvature map for DH.

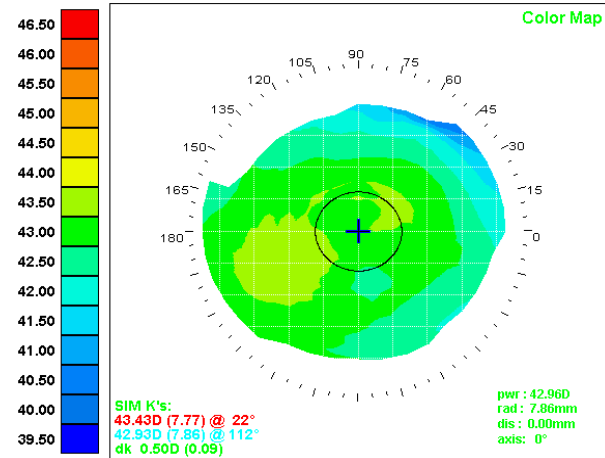


Figure 5.9 EyeSys axial curvature map for LT.

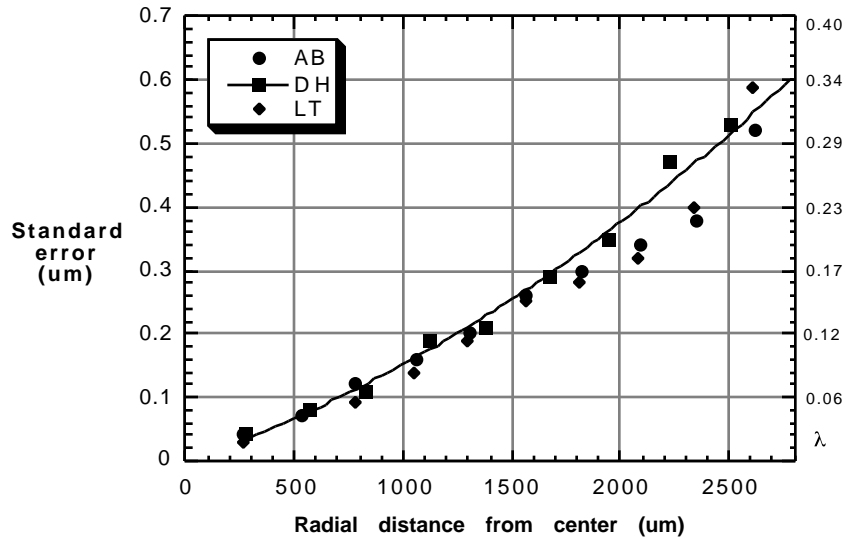


Figure 5.10

Repeatability of EyeSys surface elevation data is indicated by the radially averaged standard errors, plotted as a function of radial distance from the center. Elevation data obtained from 15-19 images were averaged to give a mean surface elevation and standard errors at approximately 4,000 points. Each ring contained 360 points, all at approximately the same radial distance from the center of the cornea. For each subject, the average of 360 standard errors within each ring are plotted.

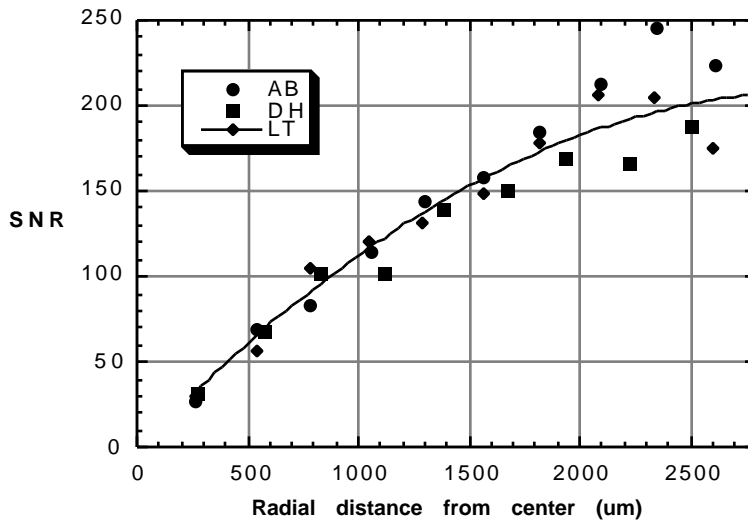


Figure 5.11

Signal-to-noise ratio (SNR) plotted as a function of radial distance from the center.

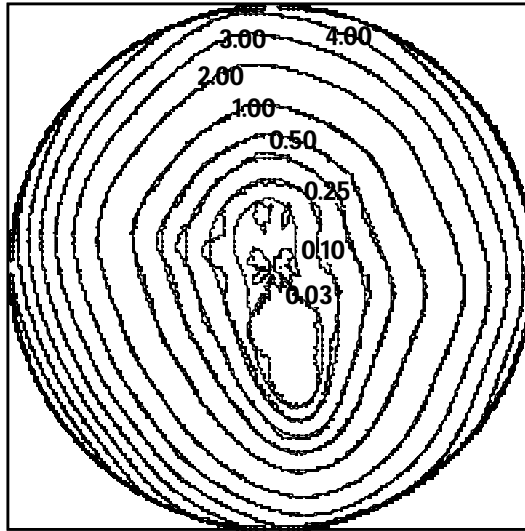


Figure 5.12

Wavefront aberrations can be computed directly from the surface elevation data, but the raw data are arranged on a slightly irregular polar grid. This was interpolated and transformed to a regular Cartesian grid for Zernike analysis. Here the contour plots for the original wavefront (EyeSys irregular polar grid), and wavefront reconstructed after Zernike analysis (evaluated at the same locations), are superimposed. Subtle wavefront irregularities, in the original data, near the center, were smoothed out by the interpolation and surface fitting process, but the difference between these and the reconstructed wavefront were less than 0.05 wavelengths. For most of the wavefront, the two contours superimpose perfectly. This indicates that the wavefront described by the Zernike coefficients closely matches the original data.

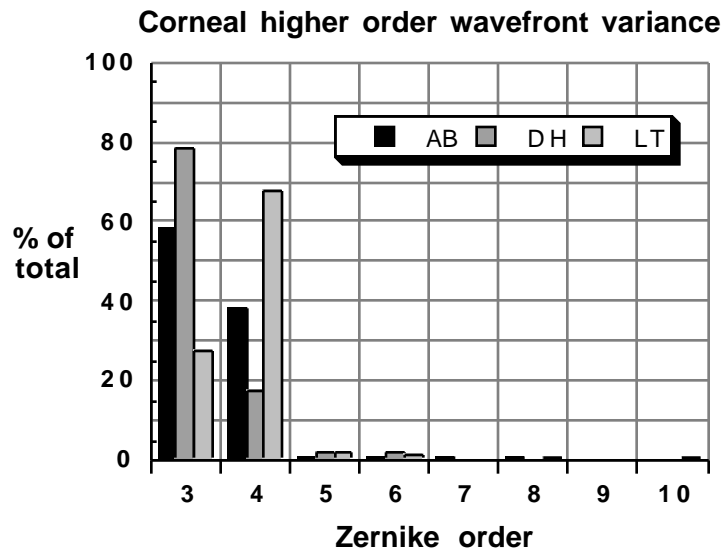


Figure 5.15

Relative contribution of each Zernike order in the corneal aberrations expressed as a percentage of the higher order wavefront variance.

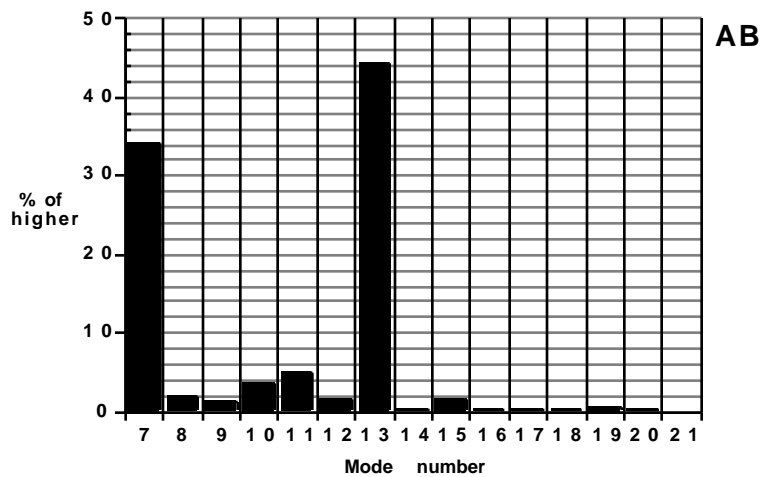


Figure 5.16

The relative contribution of the aberrations in Zernike modes 7-21 (3rd, 4th and 5th orders) for subject AB. Modes 7 and 10 combine to form triangular astigmatism. Mode 13 is primary spherical aberration. Primary coma is formed by the combination of modes 8 and 9. Modes 22-66 are not shown since they contribute very little to the higher order wavefront variance.

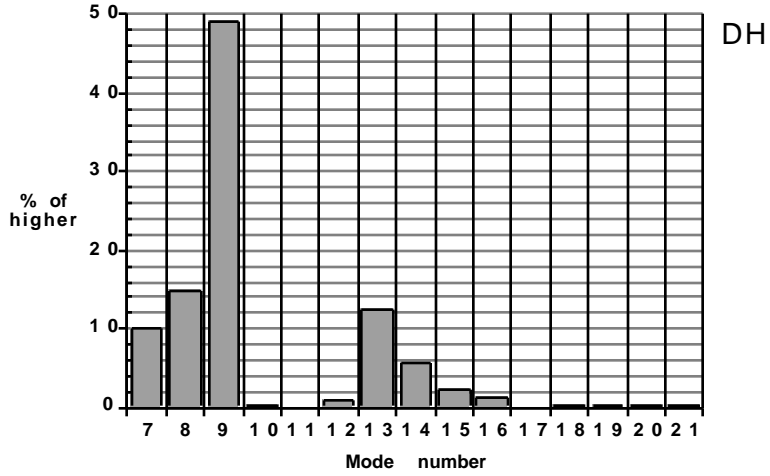


Figure 5.17

The relative contribution of the aberrations in Zernike modes 7-21 (3rd, 4th and 5th orders) for subject DH. Modes 8 and 9 combine to form primary coma. Primary spherical aberration is represented by mode 13. Modes 22-66 are not shown since they contribute very little to the higher order wavefront variance.

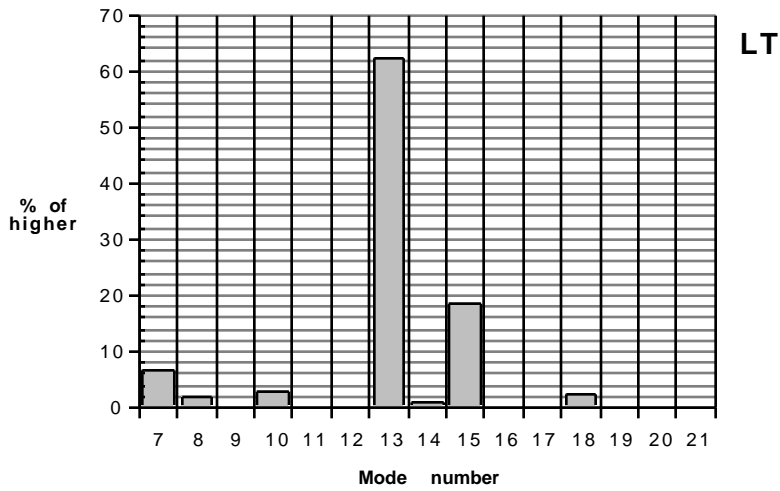


Figure 5.18

The relative contribution of the aberrations represented by Zernike modes 7-21 (3rd, 4th and 5th orders) for subject LT. Mode 13 is primary spherical aberration. Modes 22-66 are not shown since they contribute very little to the higher order wavefront variance.

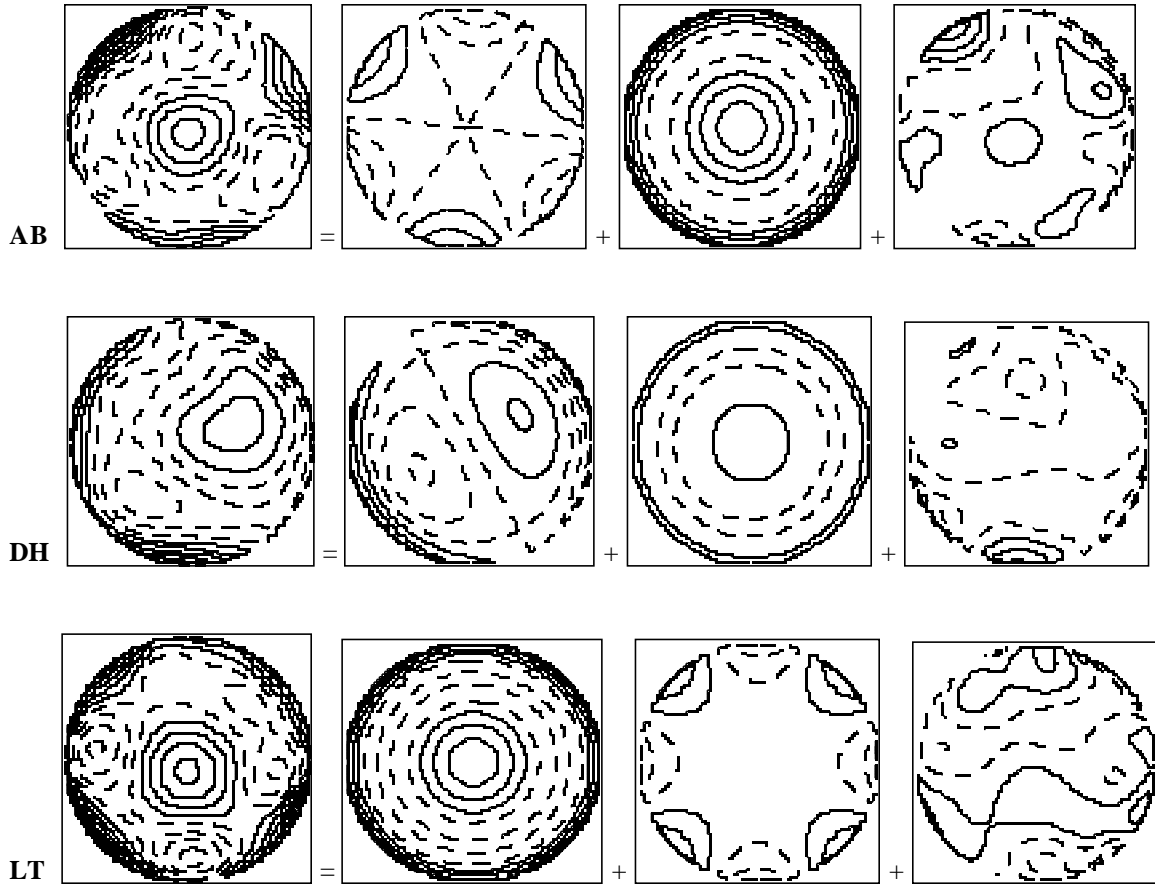


Figure 5.19

Higher order aberration components. From left to right, the plots show: for AB; total, triangular astigmatism, 1° spherical, remainder; for DH; total, 1° coma, 1° spherical, remainder; for LT; 1° spherical, quadrilateral astigmatism, remainder. The contour intervals are 0.2 ; dashed lines shows negative contours.